https://doi.org/10.1016/j.apenergy.2024.122834

A mutually beneficial system incorporating parabolic trough concentrating solar power system with photovoltaics: a comprehensive techno-economic analysis

Qiliang Wang *, Yao Yao, Yongting Shen, Zhicheng Shen, Hongxing Yang *

Renewable Energy Research Group (RERG), Department of Building Environment and Energy Engineering, The Hong Kong Polytechnic University, Hong Kong, China

---

* Corresponding author.

E-mail address: qlwang@mail.ustc.edu.cn; qiliang.wang@polyu.edu.hk (Q. Wang);

hong-xing.yang@polyu.edu.hk (H. Yang)

Abstract

The parabolic trough collector is widely recognized as the leading and mature technology for concentrated solar thermal applications, allowing for the generation of high-temperature thermal energy. However, the parabolic trough collector still faces challenges in achieving high solar-thermal efficiency due to significant radiation heat loss incurred, particularly under high operating temperatures. To address this issue and maximize the capture of solar irradiation, a novel parabolic trough collector system integrated with photovoltaic cells and a high-reflective coating was proposed. The proposed novel systems in different configurations were manufactured and tested in the indoor solar simulator laboratory to assess their feasibility and performance. Additionally, a comprehensive mathematical model regarding the novel system was developed and validated by the experiments. This study then involved assessing the potential application of the novel parabolic trough collector system in a concentrated solar power plant. And the overall techno-economic performance of the novel power plant was analyzed and evaluated for three typical areas across the globe. The results showed that the novel configurations of photovoltaic cells and high-reflective coating in the proposed system exert

excellent roles in significantly improving the efficiency of the solar irradiance utilization and reducing the radiation heat loss. Compared to the prototype power plant, the proposed power plant with the novel system possessed superior techno-economic performance, including a significant improvement of 10.1 % in annual power output, a noteworthy reduction of 87.0% in electricity consumption for annual freeze protection, and an effective reduction of 6.9 % in levelized cost of electricity.

Keywords: *Parabolic trough collector (PTC); Photovoltaic (PV); Photo-electrical/thermal;techno-economic; Concentrated Solar Power (CSP)*

Nomenclature

A	Area, m^2	**Abbreviation**	
c	Specific heat capacity, J/(kg·K)	amb	Ambient
D	Diameter, m	conv	Convection
G	Solar radiation, W/m^2	g	Glass envelope
h	Heat transfer coefficient, $W/(K·m^2)$	gl	Glass envelop in the lower half
L	Length, m	gu	Glass envelop in the upper half
m	Mass flow rate, kg/s	in	Inlet
Q	Net heat flux, W/m, W	out	Outlet
T	Temperature, K	s	Absorber
W	Width, m	th	Thermal
Greek Symbols		CRF	Capital recovery factor
η	Efficiency	CSP	Concentrated solar power
θ	Incidence angle, °	HTF	Heat transfer fluid
β	Temperature coefficient	OCC	Overnight capital cost
χ	Solar radiation coefficient	PTC	Parabolic trough collector
τ	Transmittance	PTR	Parabolic trough receiver
α	Absorptance	SSC	Solar selective-absorbing coating
ε	Emittance		

1. Introduction

Concentrated solar thermal technology is a widely adopted method for capturing high-temperature thermal energy from solar radiation [1-3]. This technology has diverse applications in fields such as concentrated solar desalination [4, 5], and concentrated solar power (CSP) [6, 7]. The

typical implementation schemes of concentrated solar thermal technology include parabolic trough collectors (PTC) [8-10], tower collectors [11-13], and Fresnel collectors [14, 15], among others [16-18]. Notably, PTC is the most established technology and has been extensively deployed globally [19]. The PTC system comprises parabolic trough receivers (PTR), highly reflective mirrors, and structural supports [20], with the PTR serving as the key component that concentrates solar rays using mirrors to achieve operating temperatures above 200°C [21]. In commercial CSP plants, the PTC system can attain operating temperatures of up to 400°C or even 550°C when utilizing thermal oil or molten salt as heat transfer fluids within the PTRs [22, 23].

Although PTC technology has achieved good popularity and technical maturity, it has been faced with a thorny problem that has not been effectively solved so far. That is the extremely high heat loss of the PTR induced by the high operating temperature [24]. According to the experimental report from the National Renewable Energy Laboratory (NREL) [25], the PTR's heat loss increases with its operating temperature raised to the fourth power, which is estimated to significantly reduce the thermal efficiency of the PTC system by 5.0~20% under the operating temperatures of 400 and 550 °C. Aiming to decrease the heat loss of the PTR and thus improve the thermal efficiency of the PTC system, the researchers have taken endeavored efforts on the solar selective-absorbing coating (SSC) for decades. SSC is generally deposited on the inner tube of the PTR for high solar radiation absorption and is a key functional material to obtain the highest possible solar energy and lose the least possible thermal energy [26, 27]. In recent years, many advanced SSCs have been developed to further reduce thermal emittance on the premise of high enough solar energy absorptance [28, 29]. Up to now, the state-of-the-art SSC used in commercials has achieved a solar absorptance of 0.96 and thermal emittance of 0.09 at the service temperature of 400 °C [30]. However, the heat loss of the PTR at 550 °C still accounts for up to 15 % of the total solar energy absorbed by the PTC system [31].

In such scenarios, novel parabolic trough receivers (PTRs) have been proposed and designed by the authors and various other researchers to more effectively mitigate heat loss compared to conventional PTR structures [10, 32]. The authors investigated the circumferential thermal flow around the PTR, revealing that the upper half of the PTR experiences negative heat gain due

to excessive heat loss exceeding the solar irradiance of one sun. Based on these findings, several innovative PTR designs have been proposed to maximize heat loss reduction at the upper half of the PTR, even if it entails sacrificing a portion of the upper one solar irradiation level. As an illustration, Yang et al. [33] proposed a novel PTR design that incorporated a secondary selective surface coating (SSC) with ultra-low thermal emissivity to replace the original SSC on the upper section of the absorber tube. Al-Ansary et al. [34] filled the PTR annulus with half-insulating material, while Wang et al. [35] introduced a metal radiation shield into the upper section of the PTR vacuum annulus. Qiu et al. [36] further replaced the metal radiation shield with solar transparent aerogel. Experimental and simulated results indicated that the aforementioned PTR designs exhibited notable heat loss reduction capabilities. Nevertheless, the new configurations utilized in these novel PTRs, such as secondary SSC, insulated material, and shields, obstruct a significant portion of the incoming solar radiation from reaching the absorber tube inside the PTR, resulting in non-negligible solar radiation loss.

To address this predicament of simultaneously reducing the heat loss and solar radiation loss of PTRs, we propose a novel PTR design that integrates photovoltaic (PV) panels and high-reflective coatings with ultra-low emittance across the entire waveband [37]. The PV panel is securely fixed onto the PTC system and positioned above the PTR. High-reflective coatings are applied to the upper half of the glass envelope of the PTR and the rear surface of the PV panels (Fig. 1). This design enables the high-reflective coatings to effectively block the thermal flux emitted from the absorber tube of the PTR, thereby mitigating heat loss. Additionally, the PV panels can fully harness the incoming solar radiation with the aid of the one-axis solar tracking mechanism of the PTC system. To the author's knowledge, no researchers have yet proposed such a similar versatile system that integrates the PTC system with PV and high-reflective coatings (PTC-PVHC) for efficient cogeneration of PV electricity and solar thermal energy.

In the previous study, the performance of the hybrid PTC-PVHC with different configurations was preliminarily explored, and the optimal configuration of such a hybrid system was determined. In this study, this PTC-PVHC will be employed in a real CSP plant. The research entails designing a novel CSP plant that incorporates the PTC-PVHC system. A solar-thermal conversion model for the

novel PTC-PVHC system is developed, along with an economic model specifically tailored for the CSP plant. The study aims to analyze and compare the overall techno-economic performance of the CSP plant when equipped with the PTC-PVHC system, which includes parameters such as thermal efficiency, photoelectrical efficiency, annual power generation, freeze protection, initial capital cost, and levelized cost of heat and energy. These performance metrics are then contrasted with the original CSP plant employing a conventional PTC system. Such a novel PTC-PVHC system exhibits superior thermo-economic performance compared to the prototype system, thereby demonstrating its excellent effectiveness and promise in perfectly integrating the PTC and PV technologies, enhancing efficiency in both PV and PTC systems as well as strengthening future applications.

2. Configuration of new CSP plant equipped with hybrid PTC-PVHC system

2.1 Configuration of the hybrid PTC-PVHC system

The schematic diagram of the hybrid PTC-PVHC system is presented in Fig. 1. The PV panel is affixed to the PTC structure using circular plates and is strategically positioned above the PTR, maintaining a specific distance of 80 mm (H_{PV}). In this study, monocrystalline PV is adopted in the proposed PTC-PVHC system [38, 39]. In order to mitigate excessive interception of incoming solar radiation, the PV panel is designed with a width (W_{PV}, 125 mm) that matches the diameter of the glass envelope (D_g, 125 mm) of the PTR. Furthermore, to enhance thermal performance, three aluminum films with an ultra-low emittance of 0.03 across the entire spectrum are meticulously selected. These films are applied to the inner and outer surfaces of the upper half section of the glass envelope, as well as the rear back surface of the PV panel. It is worth highlighting that aluminum films applied to the upper section of the glass envelope are carefully designed to not intercept the solar rays that are concentrated and reflected by mirrors below, ensuring that the concentrated solar rays can effectively reach the absorber tube without obstruction.

The implementation of these three aluminum films serves multiple purposes. Firstly, they effectively obstruct the transfer of radiation heat from the absorber tube to the glass envelope, thereby minimizing heat loss. Additionally, they reduce radiation escaping from the glass envelope to the

environment, optimizing thermal efficiency. Lastly, they prevent excessive radiation heat projection from the PTR onto the rear surface of the PV panel, safeguarding its operational integrity.

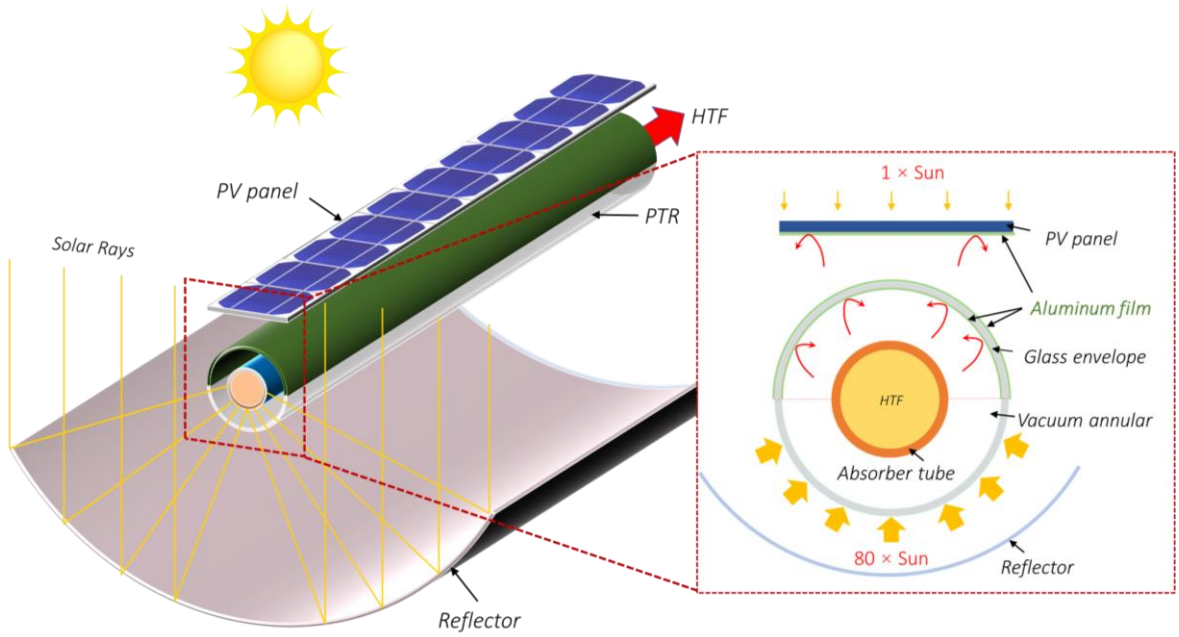

Fig. 1 Schematic diagram of the hybrid PTC-PVHC system

2.2 Configuration of the CSP plant equipped with hybrid PTC-PVHC system

Typically, a parabolic trough-type CSP system consists of several key components, including a parabolic trough solar field, thermal storage tanks, heat exchangers, and a steam turbine [40], as depicted in Figure 2(a). The solar radiation captured within the solar field is initially converted into thermal energy within the heat transfer fluid (HTF), which is then transported to the hot salt tank. Subsequently, through the heat exchanger, the thermal energy stored in the hot salt tank is transferred to water, resulting in the generation of high-temperature steam. This steam is utilized to drive a turbine, thereby producing electricity. The HTF, after transferring its thermal energy, is subsequently pumped back into the cold tank and circulated back into the solar field for the continuous collection and conversion of solar radiation. In this configuration, the HTF employed is selected as solar binary salt ($NaNO_3$-KNO_3, 60-40 wt%) [41, 42]. This particular choice of heat transfer fluid is based on its excellent stability at high temperatures of up to 600 °C, making it a widely utilized option in commercial CSP plants. The hot and cold salt tanks possess salt temperatures of 550 and 290 °C, respectively.

In this study, to investigate the techno-economic performance of the proposed PTC-PVHC system, the new PTR with PV panels, configured as Fig. 1 and Fig. 2(b), is employed in the parabolic trough-type CSP plant. The single solar field loop used in the CSP plant is shown in Fig. 2(c). It is composed of 8 solar collector assemblies (SCAs), each of which has a length of 100 m and an aperture width of 5.76 m. The original PTR and PTC adopt the commercially popular Schott 2008 PTR70 solar receiver [43, 25] and Eurotrough collector [44]. The detailed specifications of the single loop and PTC system are presented in Table 1. The concentration ratio of such a popular PTC system is calculated as 82.3 according to the dimensions in Table 1.

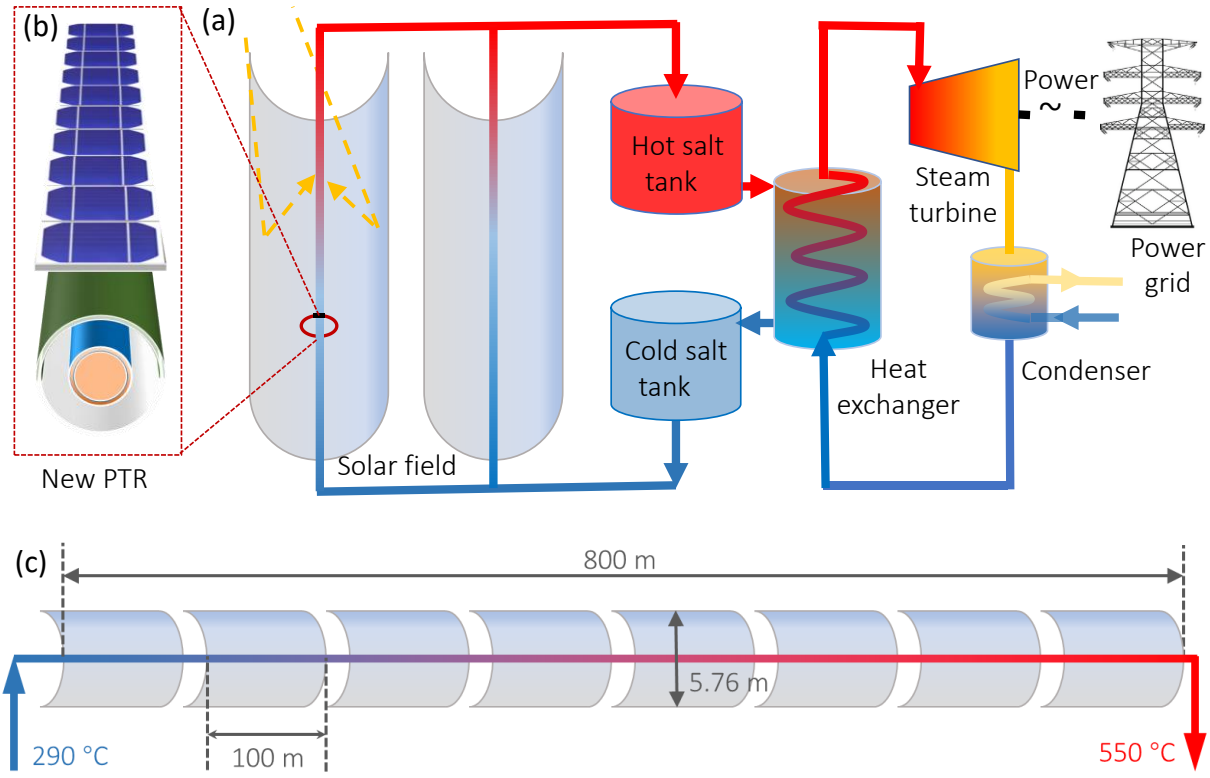

Fig. 2 Parabolic trough CSP plant system using the solar binary salt as the HTF. (a) Schematic diagram of CSP system, (b) Newly designed PTR integrated with PV, and (c) Single solar field loop in the CSP system

Table 1 Specifications of the single solar field loop and PTC system [45, 46]

Parameter	Specification	Parameter	Specification
Single SCA length	100 m	Loop optical efficiency ($\eta_{0,\,\mathrm{PTC}}$)	0.736

SCA number in single loop	8	Loop optical efficiency ($\eta_{0,\,\mathrm{PTC\text{-}PVHC}}$)	0.722
Single loop length (L_{loop})	800 m	Length of single PTR	4.06 m
Aperture width (W_{ap})	5.76 m	Diameter of absorber tube (D_{s})	70 mm
Single loop aperture area (A_{ap})	4360 m^2	Diameter of glass envelope (D_{g})	125 mm
PTR number in single loop	192	Width of PV panel (D_{PV})	125 mm
Loop inlet HTF temperature (T_{in})	290 °C	Height of PV panel (H_{PV})	80 mm
Loop outlet HTF temperature (T_{out})	550 °C		

3. Mathematical model and Methodology

3.1 Heat transfer model and photoelectrical conversion model of the PTC-PVHC system

In this study, the thermal and photoelectrical performance of the PTC-PVHC system along the loop is evaluated by employing the finite volume method. As depicted in Fig. 3, the entire loop is discretized into a series of one-dimensional finite volumes [20]. For each volume, represented by the index i (i_{th}), dedicated heat transfer and photoelectrical conversion models are formulated. These models are designed to accurately capture the intricate processes occurring within each volume, encompassing both the thermal aspects and the photoelectric conversion.

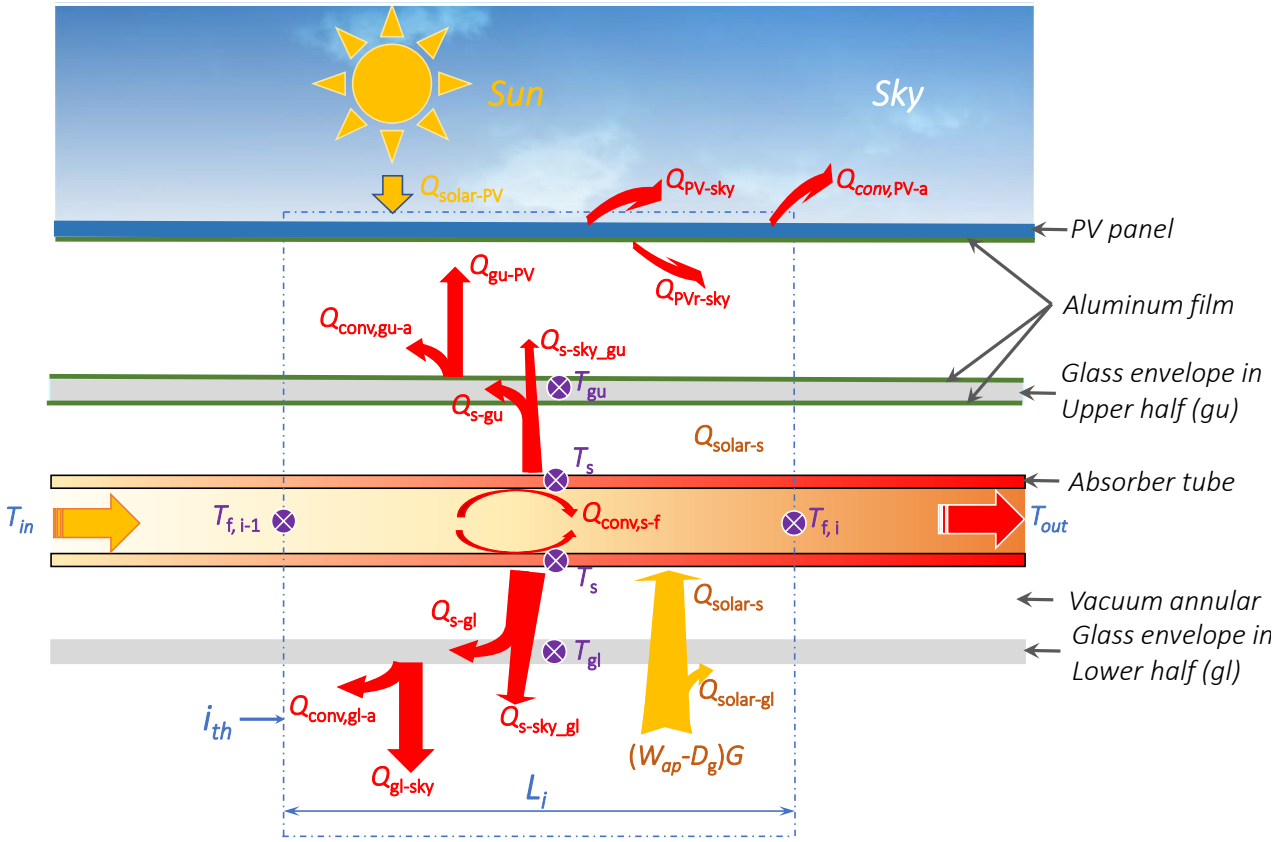

Fig. 3 Heat transfer model of the PTC-PVHC system [20, 37]

Taking into account the distinct configurations of the glass envelope in the upper half (gu) and lower half (gl), the radiation heat flux emitted from the absorber tube (s) is partitioned into two distinct components, with each component transferring heat to the corresponding section of the glass envelope (gu and gl, respectively). This division allows for a more precise characterization of the heat transfer process and ensures that the thermal distribution within the glass envelope is accurately accounted for. The expressions of heat fluxes involved in Fig. 3 are presented in Table 2. The detailed explanations of expressions can be referred to in the literature [20, 37].

Table 2 Heat fluxes involved in the PTC-PVHC in i_{th} finite volume [37]

Heat flux (W/m)	**Expressions**
Radiation heat flux between s and gu	$Q_{r,s-gu}=\dfrac{2\pi\sigma(T_s^4-T_{gu}^4)}{\dfrac{1-\varepsilon_s}{\varepsilon_s D_s}+\dfrac{1}{D_s F_{s-gu}}+\dfrac{2(1-\varepsilon_c)}{D_c A_g}}$

Radiation heat flux between s and gl	$Q_{r,s-gl}=\frac{2\pi\sigma(T_s^4-T_{gl}^4)}{\frac{1-\varepsilon_s}{\varepsilon_s D_s}+\frac{1}{D_s F_{s-gl}}+\frac{2(1-\varepsilon_g)}{\varepsilon_g D_g}}$
Radiation heat loss from gu to sky	$Q_{r,gu-sky}=\frac{\pi\sigma(T_{gu}^4-T_{sky}^4)}{\frac{2(1-\varepsilon_c)}{\varepsilon_c D_g}+\frac{2}{D_g F_{gu-sky}}}$
Radiation heat loss from gl to sky	$Q_{r,gl-sky}=\frac{\pi\sigma(T_{gl}^4-T_{sky}^4)}{2\frac{1-\varepsilon_g}{\varepsilon_g D_g}+\frac{2}{D_g}}$
Radiation heat flux between gu and PV panel	$Q_{r,gu-PV}=\frac{\pi\sigma(T_{gu}^4-T_{PV}^4)}{2\frac{1-\varepsilon_c}{\varepsilon_c D_g}+\frac{2}{D_g F_{gu-PV}}+\pi\frac{1-\varepsilon_c}{\varepsilon_c W_{PV}}}$
Radiation heat from the upper surface of the PV panel to sky	$Q_{r,PVu-sky}=\frac{\sigma(T_{PV}^4-T_{sky}^4)}{\frac{1-\varepsilon_{PV}}{\varepsilon_{PV} W_{PV}}+\frac{1}{W_{PV}}}$
Radiation heat from the rear surface of the PV panel to sky	$Q_{r,PVr-sky}=\frac{\sigma(T_{PV}^4-T_{sky}^4)}{\frac{1-\varepsilon_c}{\varepsilon_c W_{PV}}+\frac{1}{W_{PV} F_{PVr-sky}}}$
Convection heat fluxes between gu with the ambient	$Q_{conv,gu-a}=h_{amb}\pi D_g/2\,(T_{gu}-T_{amb})$
Convection heat fluxes between gl with the ambient	$Q_{conv,gl-a}=h_{amb}\pi D_g/2\,(T_{gl}-T_{amb})$
Convection heat fluxes between PV panel with the ambient	$Q_{conv,PV-a}=2h_{amb}W_{PV}(T_{PV}-T_{amb})$
Heat gain of the HTF	$Q_{conv,s-HTF}=h_{\text{s-HTF}}\pi D_s(T_s-T_{HTF})$

In Table 2, σ is the Stefan-Boltzmann constant, 5.67×10^{-8} W/(m^2·K^4) [20]. The temperatures of the absorber tube, upper-half glass surface, lower-half glass surface and sky are denoted as T_s, T_{gu}, T_{gl} and T_{sky}, respectively, K. The value of T_{sky} can be calculated by Equation (1) according to the ambient temperature (T_{amb}) [47]. The respective diameters of the absorber tube and the glass envelope are represented by D_s and D_g, m. The view factors, denoted as $F_{s\text{-}gu}$ and $F_{s\text{-}gl}$, determine the proportion of radiation heat flux emitted from the absorber tube that strikes the surfaces gu and gl, respectively. These view factors are assigned a value of 0.5. $F_{gu\text{-}sky}$ and $F_{gu\text{-}sky}$ are the view factor from the gu to the sky. Furthermore, the emittances of the SSC, aluminum coating, and glass envelope are represented by

ε_s, ε_c, and ε_g, respectively. The emittance values for the latter two are considered 0.03 and 0.89, respectively. The value of ε_s can be determined using Equation (2) based on experimental results obtained from the National Renewable Energy Laboratory [25]. h_{amb} and $h_{s\text{-}HTF}$ are the convective heat transfer coefficient to ambient, and convective heat transfer coefficient between the absorber tube and HTF, W/(K·m^2). T_{HTF} refers to the HTF temperature at the specific finite volume.

$$T_{sky} = 0.0552 T_{amb}^{1.5} \tag{1}$$

$$\varepsilon_s = 0.062 + 2 \times 10^{-7} T_s^4 \tag{2}$$

By utilizing the expressions provided in Table 2, the heat loss of the PTR (HL_{PTR}, W/m) can be obtained by the expression:

$$HL_{PTR} = Q_{r,s-gl} + Q_{r,s-gu} \tag{3}$$

Accordingly, the thermal efficiency of the PTC-PVHC system in volume i can be calculated by Equation (4).

$$\eta_{th,PTC} = {Q_{conv,s-HTF}}\Big/{(W_{PTC} \bullet G)} = \eta_{0,PTC-PVHC} - {HL_{PTR}}\Big/{(W_{PTC} \bullet G)} \tag{4}$$

where G is available solar radiation achieved by the PTC-PVHC, which can be expressed as,

$$G = I \cos\theta \tag{5}$$

where I is global solar irradiance, W; θ is the incident angle, rad. For the collector with East-West tracking and South-North direction axis, the value of θ can be calculated by the expression [43]:

$$\begin{cases} \cos\theta = \sqrt{\cos^2\theta_z + \cos^2\delta \sin^2\omega} \\ \cos\theta_z = \sin\phi \sin\delta + \cos\phi \cos\delta \cos\omega \end{cases} \tag{6}$$

where δ, ϕ, θ_z, and ω are the solar declination angle, latitude, zenith angle, and solar angle, respectively. Due to the constraints of the study's length, the detailed expressions for calculating these parameters are not provided, they can be referred to the references [48, 49].

After this calculation process, thermal energy obtained by the HTF ($Q_{gain,\,i}$, W) in volume i and total thermal energy in a single loop (Q_{gain}, W) can be expressed in Equations (7) and (8) [40]:

$$Q_{gain,i} = \dot{m} c_{p,i} (T_{f,i} - T_{f,i-1}) \tag{7}$$

$$Q_{gain} = \sum_{i=1}^{j} L_i \bullet Q_{gain,i} \tag{8}$$

where m and c_p are the mass flow rate and specific heat of the HTF, respectively, kg/s, J/(kg·K). In this study, the value of m is assumed to be 5.0 kg/s, and the specific property parameters of the molten salt, including c_p, can be sourced from relevant literature references [50].

Finally, the thermal efficiency of a single PTC-PVHC loop can be calculated by Equation (9).

$$\overline{\eta_{th,PTC}} = Q_{gain} \Big/ (A_{ap} \bullet G) \tag{9}$$

Besides the thermal performance of the PTC-PVHC system, the model regarding the photoelectric performance of the PV panel is also developed. The available solar energy used by the PV panel is expressed as,

$$Q_{solar-PV} = W_{PV} \tau_{PV} \alpha_{PV} I \cos\theta \tag{10}$$

where τ_{PV}, α_{PV} and ε_{PV} represent the solar transmittance of the tempered glass, solar absorptance, and the thermal emittance of the PV layer. The respective values assigned to these parameters are 0.95, 0.97, and 0.97. Using the heat transfer fluxes listed in Table 2, the temperatures of the upper-half glass surface (gu), lower-half glass surface (gl), and PV layer can be determined through the application of the energy balance method.

Furthermore, the electrical efficiency of the PV cell (η_{PV}) can be obtained by employing the fundamental equation [51]:

$$\eta_{PV} = \eta_{Tref} [1 - \beta_{ref} (T_{PV} - T_{ref}) + \chi \log_{10} G] \tag{11}$$

In the aforementioned equation, η_{Tref} represents the electrical efficiency of the PV cell at the reference temperature (T_{ref}) and under a solar radiation of 1000 W/m^2. The temperature coefficient (β_{ref}) and solar radiation coefficient (χ) are two parameters that describe the material properties of the PV cell. For crystalline silicon, typical values for β_{ref} and χ are 0.0045 K and 0.12, respectively. The effective solar

irradiance projected on the PV panel, denoted as G, is measured in W/m^2. At the standard test condition, G is typically set at 1 kW/m^2.

3.2 Economic assessment model of the CSP plant

To evaluate the economic viability of the CSP plant incorporating the PTC-PVHC system, an economic assessment model is formulated in this section. The costs associated with PTC-PVHC systems typically encompass initial investment, operation, and maintenance expenses. In this study, the Levelized Cost of Energy (LCOE) metric is employed to analyze and compare the economic performance of the original PTC and the PTR-PVHC configuration.

(1) Initial investment

The initial investment of the PTC-PVHC plant primarily comprises various components, including the ground field (site improvements), solar field, thermal storage, HTF, power block, and fossil/heater backup [52, 53]. The solar field cost and HTF cost are calculated based on the cost per square meter of the solar field area, which accounts for expenses associated with the installation of the solar field and the pumps and piping, respectively. It is important to note that the costs of the solar field differ depending on whether the PTC or PTC-PVHC configuration is employed. In particular, the manufacturing cost of the PTC-PVHC is approximately 10 % higher than that of the PTC, as determined from real manufacturing experience and data.

The thermal storage cost refers to the expense per thermal kilowatt (kWt) of storage capacity, encompassing the installation costs of the thermal storage system. Similarly, the power block cost represents the cost per electric kilowatt (kWe) of power block gross capacity, accounting for the installation of the power block. It is important to note that all of the aforementioned costs include both labor and equipment expenses. The inclusion of a fossil/heater backup system is an essential component in Concentrated Solar Power (CSP) plants, serving the purpose of mitigating heat losses in the Heat Transfer Fluid (HTF) during nighttime and off-hours. This backup system prevents a decline in temperature and the potential occurrence of freezing within the solar field. In line with the empirical parabolic trough CSP plant, Table 2 provides a breakdown of the specific costs considered for calculating the initial investment cost of the plant.

Table 3 Initial investment cost [54, 55]

Initial investment category	Unit cost (USD)
Ground field	25 \$/m^2 (Land area)
Solar field with the PTC/PTC-PVHC	150 / 155 \$/m^2 (Collector aperture area)
HTF system	60 \$/m^2
Thermal storage	62 \$/kWt
Power block	910 \$/kWe
Fossil/Heater backup	30 \$/kWe

(2) Operation and maintenance costs

Operation and maintenance costs encompass the recurring annual expenditures associated with equipment and services necessary for the functioning of the plant system. In this study, the average fixed operation and maintenance costs are primarily composed of three components: fixed cost by capacity and variable cost by generation, along with the inclusion of insurance expenses. The fixed cost by capacity is determined to be 66 \$/kW-year, while the variable cost by generation is calculated as 4 \$/MWh, as referenced in [56]. The determination of insurance expenses can be achieved by employing the following expression:

$$IE_i = I_{install} \bullet R_{insurance} \bullet (1 + R_{inflation})^{i-1} \tag{12}$$

where IE_i represents the insurance expense in year i, $I_{install}$ is the total installed costs of parabolic trough CSP plant, \$. $R_{insurance}$ and $R_{inflation}$ are the insurance rate and inflation rate which are determined as 0.5 and 2.5 %, respectively.

(3) Levelized cost of heat and energy (LCOH and LCOE)

The levelized cost of heat and energy (LCOH and LCOE) serve as valuable metrics for conducting economic comparisons among various parabolic trough CSP plants. It is important to note that lower LCOH and LCOE signifie superior economic performance achieved by a parabolic trough CSP plant in terms of heat energy and electricity energy. Given an assumed operating lifetime of 25 years for the

parabolic trough CSP plant, the LCOH and LCOE can be calculated using the following equations, as referenced in [57-59]:

$$LCOH = \frac{OCC \bullet CRF + OM}{H} \tag{13}$$

$$LCOE = \frac{I_0 + (\sum_{i=1}^{j} I_i + OM_i + FH_i)/(1+R_{discount})^i}{(\sum_{i=1}^{j} E_i)/(1+R_{discount})^i}, \tag{14}$$

where OCC, CRF and H are the overnight capital cost, capital recovery factor and heat energy produced, respectively. I_0 is the initial investment, I_i, OM_i, and FH_i are the investment expenditures, operation and maintenance expenditures, and fossil/heater expenditures in the year i, respectively. E_i represents the electricity generated by the CSP system in year i. The variable j denotes the lifetime of the system. Furthermore, $R_{discount}$ represents the discount rate utilized in discounted cash flow analysis, which is the interest rate used to determine the present value of future cash flows. For this particular study, the value of $R_{discount}$ is set at 6.4% [60, 52].

4. Test rig and expermental validaiton

4.1 Test rig, experiments and methodology

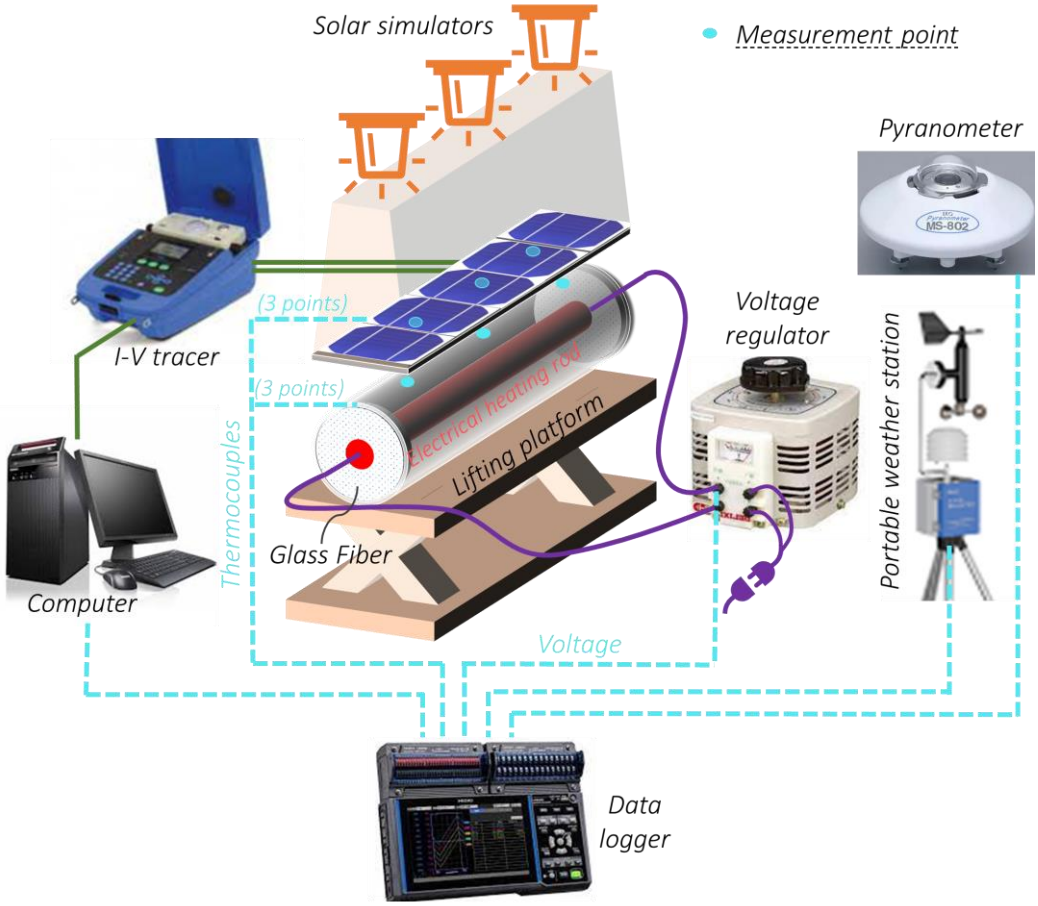

Fig. 4 Schematic of the PTC-PV experimental system

In this study, a test rig of the PTC-PVHC system was established in the indoor solar simulator laboratory at Hong Kong Polytechnic University to validate the predictive capability of the mathematical model. The simplified test rig is illustrated in Fig. 4. The solar simulator employed in the laboratory is capable of generating a solar spectrum similar to that emitted by the outdoor Sun [61-63]. The customized PTC-PVHC device was positioned on a lifting platform, allowing for adjustable heights to achieve desired solar irradiances. It is noteworthy that the parabolic trough reflector is omitted in the customized PTC-PVHC system. This experimental configuration was proposed considering technical effects and operational ease. Technically, the reflector primarily concentrates solar rays onto the lower half part of the PTR, which does not affect the functionality of the special components incorporated in the PTC-PVHC system, namely the PV panel and the high-reflective coating situated on the upper half part of the PTR. From an experimental perspective, this simplified

configuration facilitates easier and more efficient experimental operations. Thus, the adoption of such a simplified experimental configuration for the PTC-PVHC system is deemed reasonable and acceptable.

To examine the influence of glass temperature on the thermal performance of the PTR and PV panel's performance, an electrical heating rod was inserted into the PTR, serving as the inner absorber tube. By adjusting the voltage, the glass temperature could be precisely controlled. A total of 6 thermocouples were affixed to the glass envelope and the rear side of the PV panel to monitor the temperatures of the glass and PV panel. Throughout the operation, various environmental parameters including solar irradiance, ambient temperature, and wind speed were measured using a pyranometer and a portable weather station. The PV performance was assessed using an I-V checker. All monitored data were subsequently transmitted and recorded by a Data Logger for further analysis. Throughout the experimental process, the temperature of the glass envelope was increased from the ambient temperature to approximately 150 °C, enabling the testing and calculation of relevant performance metrics. The power output of the PV panel (P_{PV}) was determined by multiplying the monitored current and voltage values, thereby allowing the calculation of PV efficiency (η_{PV}) [64, 24].

$$P_{PV} = IV \tag{15}$$

$$\eta_{PV} = {P_{PV,m}}/{GA_{PV}} \tag{16}$$

where $P_{PV,m}$ represents the maximum power output, W; A_{PV} refers to the area of the PV panel, m^2.

In this study, two different modes of the PTC-PVHC system were manufactured and tested to assess their overall performance and validate the predictive capability of the mathematical models developed in Section 3. The modes are illustrated in Fig. 5 and their distinctions are presented in Table 4. Mode A involves the addition of a PV panel above the PTR, without the inclusion of an aluminum coating. Mode B, on the other hand, incorporates the aluminum coating, which is deposited on the rear side of the PV panel. Experimental rigs corresponding to these modes are depicted in Fig. 6.

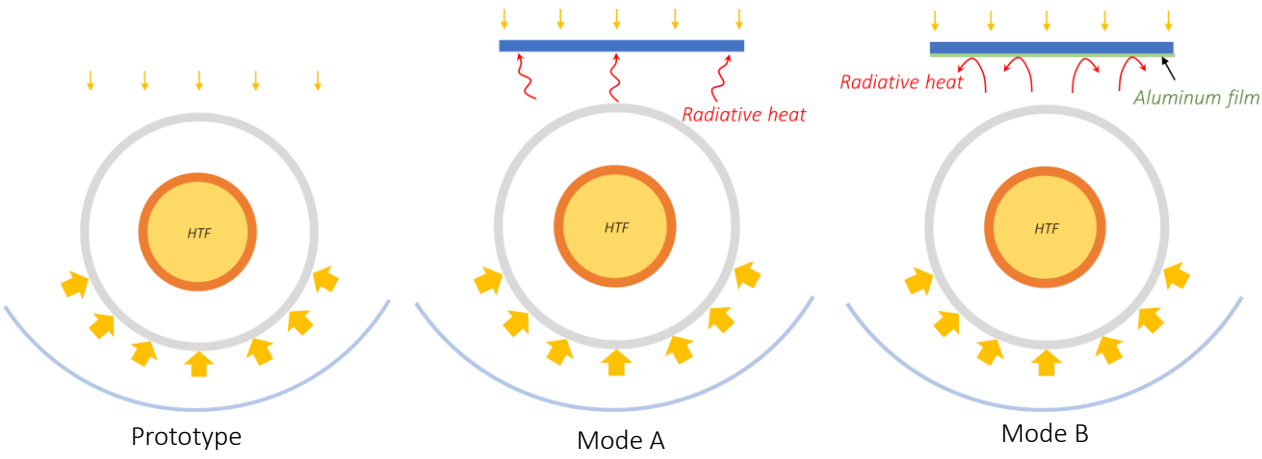

Fig. 5 Schematic diagrams of the PTC prototype system and two modes of the hybrid PTC-PV systems

Table 4 Distinctions of different modes (× and √ mean non-included and included, respectively)

Type	Prototype	Mode A	Mode B	Current Mode
PV panel	×	√	√	√
Aluminum coating (the rear of the PV panel)	×	×	√	√
Aluminum coating (glass envelope)	×	×	×	√

Following the completion of experiments involving the PTC prototype, experimental tests were conducted on PTC-PVHC systems in Modes A and B. The obtained experimental data was utilized to validate the simulation results. Subsequently, the overall performance of the PTC-PVHC system in the current mode (as depicted in Fig. 1) will be investigated numerically.

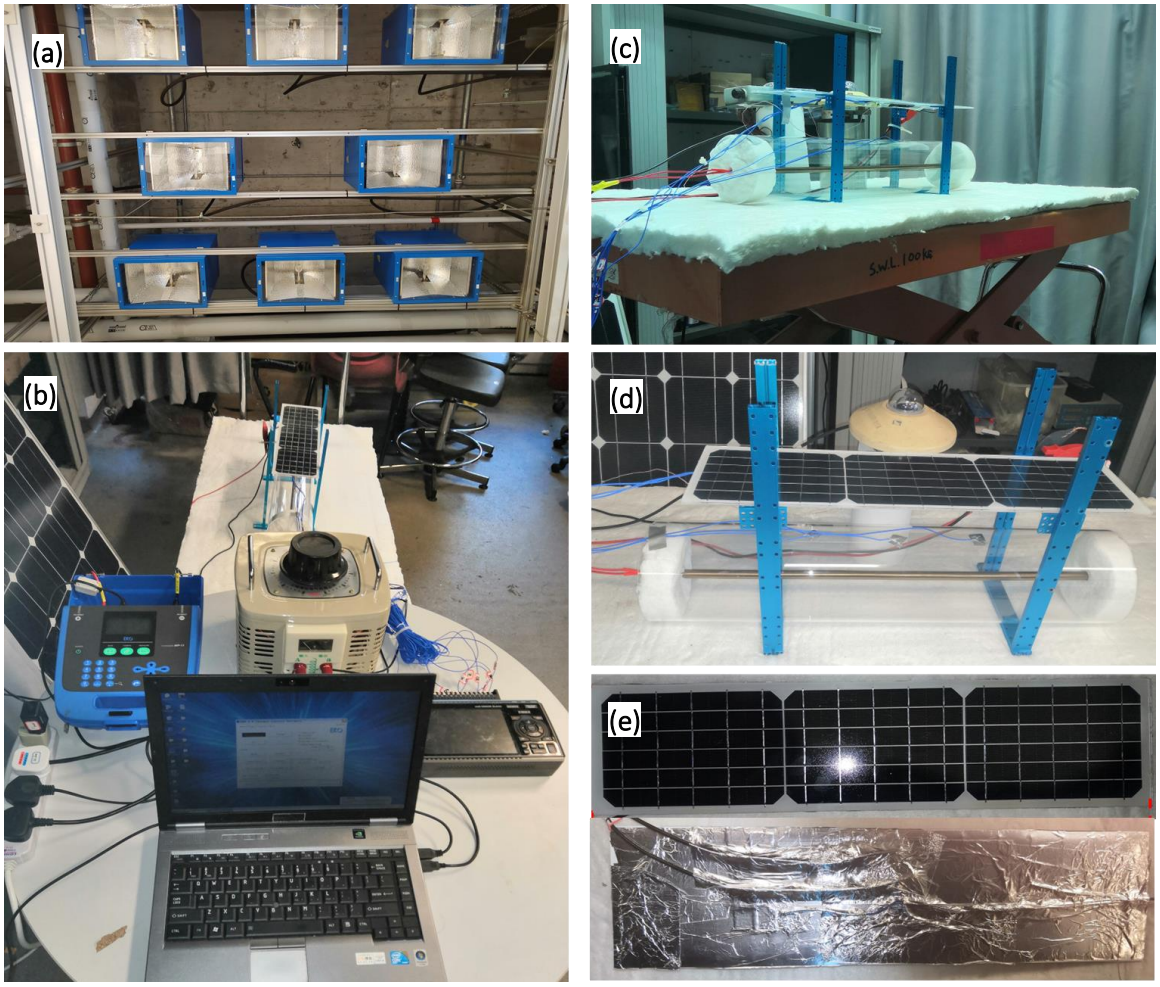

Fig. 6 Built test rigs in the indoor solar simulator laboratory at The Hong Kong Polytechnic University. (a) Solar simulators; (b) Panorama of the test rig; (c) Experiments of PV panel integrated PTR on the lifting platform; (d) Aerial view of the PV panel integrated PTR; (e) Monocrystalline PV panel with the rear surface coated by aluminum film

4.2 Simulated results and experimental validation

The customized PV panel underwent testing under standard conditions, where the solar radiation was approximately 1000 W/m^2. The resulting I-V curve is presented in Fig. 7. Notably, the PV temperature during the test was 35.9 °C. The short-circuit current (I_{sc}) and open-circuit voltage (V_{oc}) were measured as 3.84 A and 3.78 V, respectively. The PV panel achieved a maximum power output ($P_{PV,\,m}$) of 10.45 W, yielding an electrical efficiency of approximately 16.5%. The detailed metrics of the PV panel are shown in Table 5.

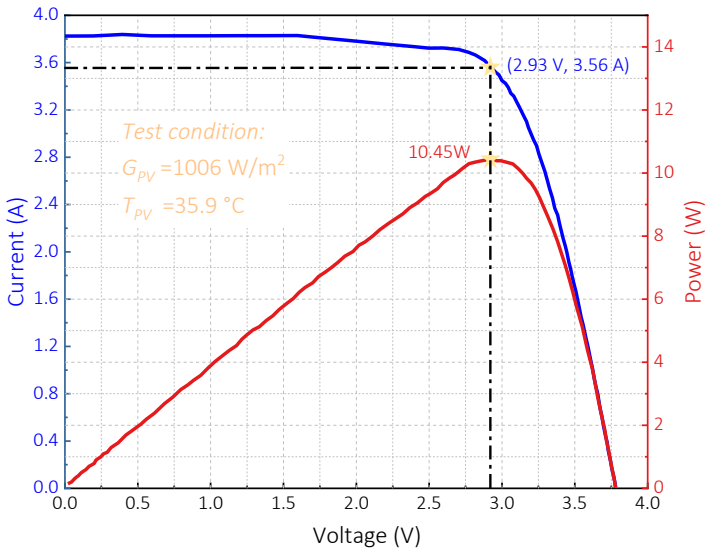

Fig. 7 Tested I-V curve of the PV panel

Table 5 Key performance parameters of the monocrystalline PV panel used in the test

Parameter	I_{sc}	V_{oc}	$P_{pv,\,m}$	η_{pv}
Value	3.84 A	3.78 V	10.45 W	16.45 %

The experimental data and simulated results are depicted in Fig. 8. Upon comparing the outcomes for Modes A and B, notable observations can be made. Mode B, incorporating the aluminum coating configuration, exhibits a substantial reduction in PV temperature at elevated glass temperatures. Additionally, it demonstrates a significant enhancement in PV efficiency. These findings highlight the remarkable impact of the aluminum coating in Mode B, effectively impeding thermal emission from the PTR. As a result, the serving temperature of the PV panel is reduced, leading to improved efficiency.

Moreover, Fig. 8 (a) and (b) illustrate the close correspondence between the simulated results and experimental data regarding PV temperature and PV efficiency as the glass temperature increases. And, Fig. 8 (c) demonstrates a satisfactory alignment between the simulated heat loss of the PTR and the corresponding experimental data obtained from NREL [25]. This agreement further strengthens the validity of the simulation model. To evaluate the deviation of the simulated results, the root-mean-square deviation (*RMSD*) is used in this study [65],

$$RMSD = \sqrt{\frac{\sum[(Y_{sim,i} - Y_{\exp,i})/Y_{\exp,i}]^2}{x}} \tag{17}$$

where Y_{sim} and Y_{exp} are the simulated and experimental data, respectively, x is the number of data. The calculated values of *RMSD* for the simulation results, encompassing PV temperatures and PV efficiencies in Modes A and B, as well as PTR heat loss, all fall within 5%. This indicates that the mathematical model employed in this study exhibits exceptional predictive capability.

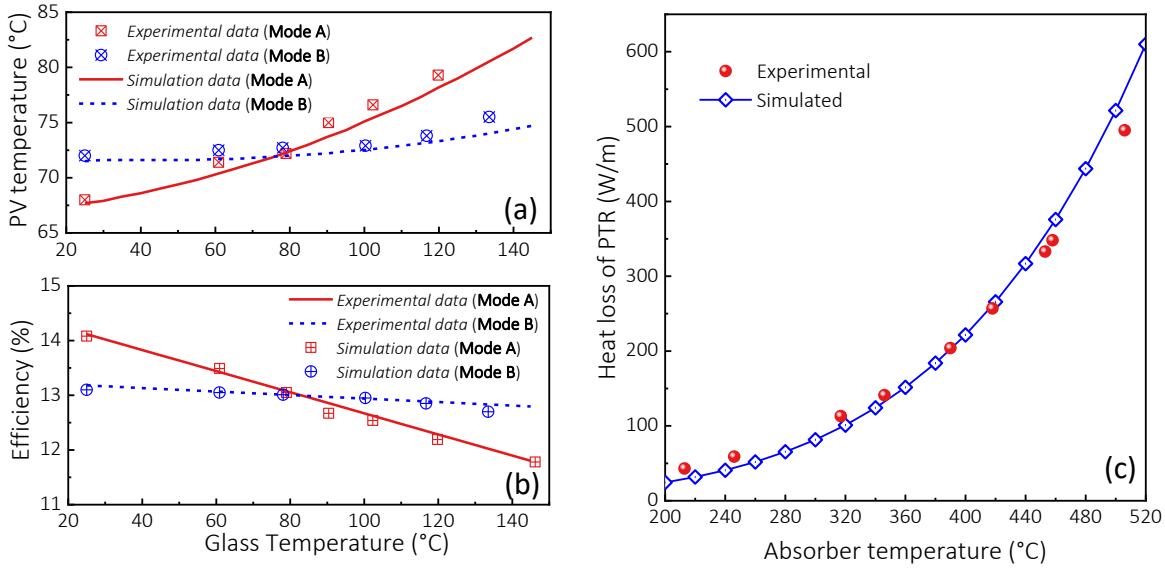

Fig. 8 Simulation results verified by experiments carried out in the indoor solar simulator laboratory.

5. Results and discussions

5.1 PTR's and PV's performance in the proposed hybrid PTC-PVHC system

Table 6 PV's performance and comparisons of three kinds of modes

T_g	*Mode A*			*Mode B*			*Current Mode*			*Relative improvement ratio (P_{PV} and η_{PV})*	
	T_{PV}	P_{PV}	η_{PV}	T_{PV}	P_{PV}	η_{PV}	T_{PV}	P_{PV}	η_{PV}	*Compared to Mode A*	*Compared to Mode B*
25	67.7	5.91	14.12	71.5	5.49	13.18	70.0	5.67	13.53	-4.1	3.3
40	68.6	5.78	13.83	71.6	5.47	13.13	70.1	5.65	13.48	-2.2	3.3
55	69.8	5.65	13.54	71.6	5.45	13.08	70.2	5.63	13.44	-0.4	3.3
70	71.3	5.53	13.25	71.8	5.43	13.04	70.3	5.62	13.39	1.6	3.5
85	73.0	5.40	12.96	72.1	5.41	12.99	70.5	5.60	13.35	3.7	3.5
100	75.1	5.28	12.67	72.5	5.39	12.94	70.7	5.58	13.30	5.7	3.5
115	77.3	5.15	12.38	73.1	5.36	12.89	71.0	5.56	13.26	8.0	3.7
130	79.9	5.02	12.09	73.8	5.34	12.84	71.4	5.54	13.21	10.4	3.7
145	82.7	4.90	11.80	74.7	5.32	12.80	71.7	5.53	13.17	12.9	3.9

Based on the experimental validations of the PTC-PVHC system in Modes A and B, as discussed in Section 4.2, the mathematical model established in this study has demonstrated excellent predictive ability. Building upon this foundation, a numerical investigation was conducted on the hybrid PTC-PVHC system in its current mode, as illustrated in Fig. 1. The findings of this investigation are summarized in Table 6 and Table 7. It should be noted that T_{PV} is the average value of three temperature points measured on the PV panel which are shown in Fig. 4.

Table 6 reveals that the current mode and Mode B exhibit higher PV temperatures compared to those in Mode A when the glass temperature approximately remains below 70 °C. However, as the glass temperature surpasses 70 °C, the PV temperatures in the current mode and Mode B change to be lower than those in Mode A. The reason for this phenomenon is the double-sided functionality of the aluminum coating on the rear back of the PV panel at different serving temperatures. On one hand, when the operating temperature of the glass envelope remains below 70 °C, the low thermal emittance of the aluminum coating impedes the dissipation of thermal radiation from the PV panel to the environment. As a result, both the current mode and Mode B exhibit higher PV temperatures compared to Mode A. On the other hand, when the glass envelope temperature exceeds 70 °C, the glass envelope emits a greater amount of radiation onto the rear surface of the PV panel. In this scenario, the aluminum coating plays a crucial role in reflecting the incoming thermal radiation from the glass envelope. Consequently, the PV panel temperatures in Mode B and the current mode start to decrease below that of Mode A. Furthermore, in the current mode, with the aid of the aluminum coating on the glass envelope, the glass emits significantly less thermal radiation than in Mode B. Consequently, the PV temperature in the current mode experiences further reduction compared to Mode B. Through the data of last two columns of Table 6, it can be observed that, with the growing operating temperature of the glass envelope, the PV power output (P_{PV}) and PV efficiency (η_{PV}) in the current mode have an increasing improvement rate and a relatively stable improvement rate compared to Modes A and B, respectively. Specifically, when the glass temperature reaches approximately 145 °C, the relative improvement rates of PV output and efficiency, compared to Modes A and B, are 12.9% and 3.9%, respectively. These results indicate that the proposed PTC-PVHC system in the current mode exhibits superior photoelectrical performance at higher operating temperatures of the glass envelope, in contrast to Modes A and B. Furthermore, these results demonstrate the effectiveness of the aluminum coatings deposited on the rear surface of the PV panel and glass envelope in minimizing the projection of thermal radiation onto the PV panels.

Besides the photoelectrical performance, the thermal performance of the PTR inside the PTC-PVHC in the current mode is also investigated. The detailed heat loss of the PTRs in three kinds of

PTC-PVHC systems is presented in Table 7. Compared to the prototype PTC system, the PTRs of the PTC-PVHC system in Modes A and B have slight reductions in heat loss due to the existence of the PV panel which can intercept a portion of the thermal dissipation from the PTR. In contrast, the PTR in current mode achieves a remarkable decrease in heat loss. This reduction is attributed to the presence of an aluminum coating on the upper part of the glass envelope, which acts as a barrier, effectively blocking the thermal emission from the absorber tube inside PTR. Overall, the PTC-PVHC system in the current mode exhibits exceptional thermal performance compared to the prototype and Modes A and B. With increasing absorber temperatures from 200 to 600 °C, the PTC-PVHC system in the current mode is capable of reducing heat loss by an impressive 30% to 45%.

Table 7 Heat loss of the PTRs in different modes

T_s	HL_{PTR}				*Relative reduction ratio*		
	Prototype	*Mode A*	*Mode B*	*Current Mode*	*Compared to Prototype*	*Compared to Mode A*	*Compared to Mode B*
200	24.4	24.2	22.4	15.4	36.9	36.4	31.3
300	81.5	81.3	75.2	49.1	39.8	39.6	34.7
400	221.6	220.9	201.5	128.8	41.9	41.7	36.1
500	521.5	519.0	491.1	295.7	43.3	43.0	39.8
600	1097.4	1090.6	1035.2	612.7	44.2	43.8	40.8

5.2 Photoelectrical and thermal performance of the PTC-PVHC system in real applications

Based on section 5.1, the PTC-PVHC system is further assumed to be applied to a real collector loop explained in Fig. 1 and Table 1 to evaluate the photoelectrical and thermal performance metrics of such a novel configuration. The collector loop in this study is equipped with an East-West tracking mechanism.

In practical applications of the PTC-PVHC system, the PV panel is designed to rotate along with the PTC system, utilizing a one-axis solar tracking mechanism. This configuration allows the PV panel to continuously adjust its orientation throughout the day, effectively reducing the cosine loss associated with the incident solar radiation. As a result, the PV panel can maintain higher photoelectrical

performance levels, optimizing energy capture and conversion throughout the entire day. In this section, typical meteorological days, i.e., summer solstice and autumnal equinox, are selected as the study cases. The results of the daily average cosine of the PV panels mounted on the PTC-PVHC and ground are depicted in Fig. 9(a). It can be observed that the cosine values of the PV panel in the PTC-PVHC in both summer solstice and autumnal equinox reach 0.993 and 0.949, which are effectively improved by 37.5 and 20.7% compared to that in the PV panel fixed on the ground, respectively. Those prove the advancement of such a hybrid PTC-PVHC system in reducing cosine loss. Furthermore, the PV efficiency varied with different solar irradiances are explored and shown in Fig. 9(b). With the increase of the solar irradiance from 300 to 1000 W/m^2, both PV panels mounted on the PTC-PVHC system and ground harvest increased efficiencies. And the former has an increasingly higher PV efficiency compared to the latter because of its much higher cosine value. The efficiency of the PV panel in the PTC-PVHC reaches 13.63 % at the solar irradiance of 1000 W/m^2, which is relatively enhanced by 14.7 % compared to that on the ground.

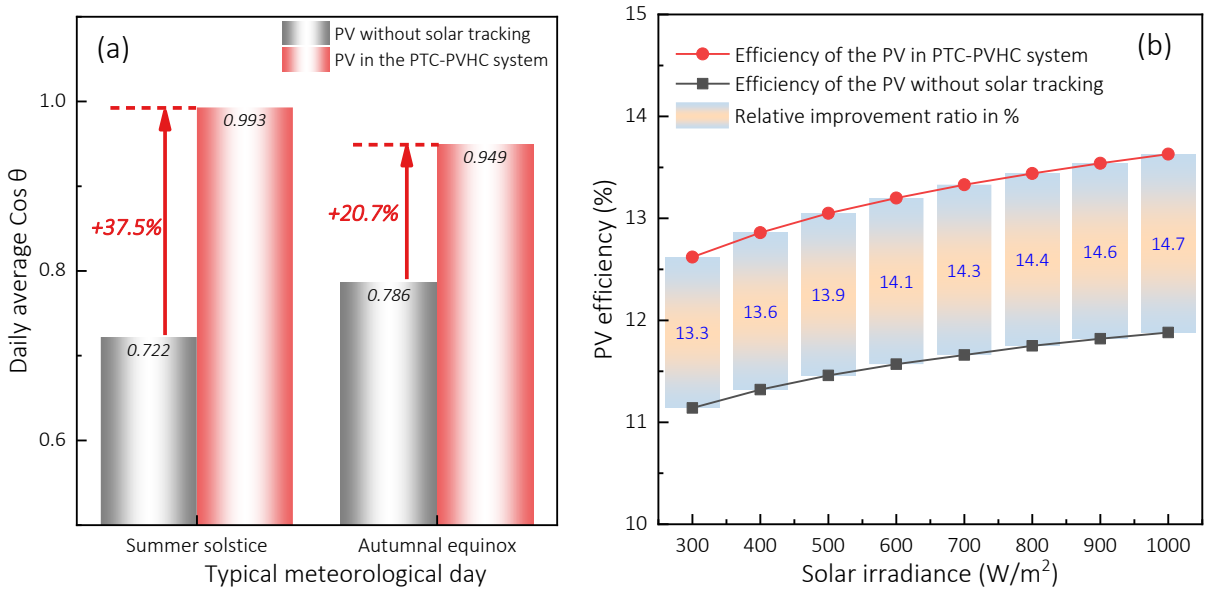

Fig. 9 Photoelectrical performance of the PV panels on the ground without solar tracking and proposed PTC-PVHC system with one-axis solar tracking. (a) Daily average cosine value; (b) PV efficiency.

To further evaluate the thermal metrics of such a hybrid system in different time buckets and solar irradiance, its loop heat loss of the PTRs and thermal efficiency are calculated and exhibited in Fig. 10 (a) and (b). During the daytime, the collector loop generally operates at high operating temperatures,

the configurations of the PTC-PVHC system, i.e., aluminum coating and PV panel, contribute significantly to a substantial reduction in heat loss by 42.9 % compared to the prototype PTC system. During the nighttime, the PTR needs to maintain above 220 °C to prevent the High-Temperature Fluid (HTF) of molten salt from freezing. In this scenario, the hybrid PTC-PVHC system can thereby continue to play an effective role in reducing the heat loss of the PTR by 39.9 %. Furthermore, it can be seen from Fig. 10 (b) that the thermal efficiencies of both hybrid PTC-PVHC and prototype PTC systems increase with the growth of solar irradiance. However, the former has a decreasing efficiency improvement compared to the latter, that is because the increasing solar irradiance causes a larger solar absorption loss for the PTC-PVHC system due to the interception of the PV panel, thereby leading to a reduced thermal efficiency improvement compared to the prototype PTC system. In the scenario of low solar irradiance of 300 W/m^2, the hybrid PTC-PVHC system can effectively improve thermal efficiency by 9.6 % compared to the prototype PTC system.

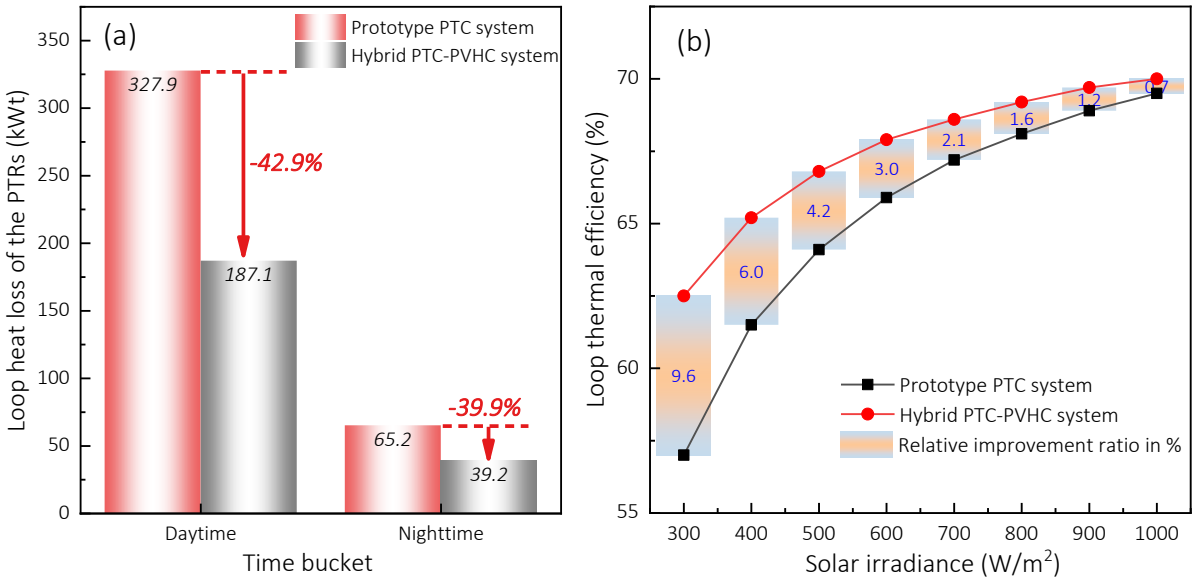

Fig. 10 PTRs' heat loss and thermal efficiency of the prototype PTC system and hybrid PTC-PVHC system. (a) Loop heat loss in daytime and nighttime; (b) Loop thermal efficiency

5.3 Configuration and overall performance of the PTC-PVHC system-based 50 MWe CSP plant

The comprehensive analysis of the PTC-PVHC system's performance discussed above has led to the design and study of a CSP plant integrated with the PTC-PVHC system. The CSP plant is

specifically configured with a power capacity of 50 MWe. To evaluate the performance of the PTC-PVHC system-based CSP plant, calculations have been conducted considering a nominal normal irradiance of 600 W/m^2. The preliminary results of these calculations, including the system configurations and performance metrics, are presented in Table 8. For the PTC-PVHC system-based CSP plant, the power capacity of 50 MWe is composed of a solar-thermal power capacity of 48.2 MWe and a PV power capacity of 1.8 MWe after calculations. Since the PTC-PVHC system-based CSP plant has a higher thermal efficiency (as explained in Fig. 10(b)) and lower solar-thermal power capacity, the loop number needed in the novel CSP plant is lower than that in the conventional CSP plant. And the electrical consumption for nominal field freeze protection in the former is accordingly reduced to 5252.8 kWe from 9323.6 kWe in the latter.

Table 8 Configurations and performance of the CSP plants with prototype PTC and hybrid PTC-PVHC systems

Item/Metric	**Prototype PTC system-based CSP plant**	**Hybrid PTC-PVHC system-based CSP plant**
Total power capacity (MWe)	50	
Turbine efficiency of power cycle (%)	40.7	
Nominal normal irradiance (W/m^2)	600	
PV efficiency (Standard condition)	\	16.5
Solar-thermal power capacity (MWe)	50	48.2
Photovoltaic power capacity (MWe)	0	1.8
Thermal power of power cycle (MWt)	122.9	118.4
Loop thermal efficiency (%)	65.9	67.9
Number of loops	143	134
Loop thermal power (MWt)	1.72	1.91
Loop mass flow rate (kg/s)	4.95	5.07

Total aperture area of solar field (m^2)	623480	584240
Nominal field freeze protection (kWe)	9323.6	5252.8

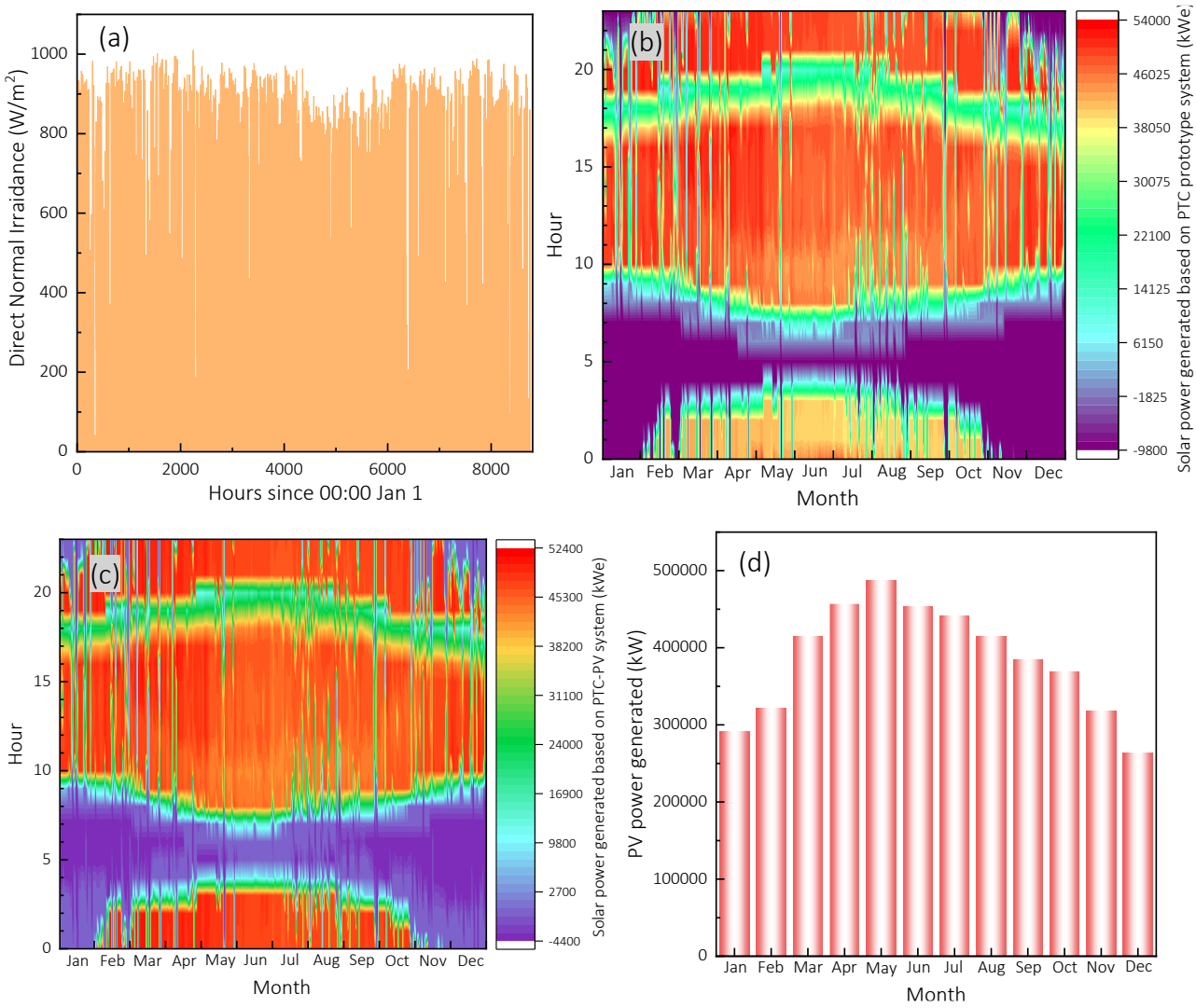

Fig. 11 (a) Annual direct normal irradiance of Phoenix, (b) Solar-thermal power output of the CSP plant with the PTC prototype system, (c) Solar-thermal power output of the CSP plant with the PTC-PVHC system, and (d) Power output of the PV arrays in the PTC-PVHC system.

Based on the above configuration, the techno-economic performance of the two kinds of CSP plants is studied and analyzed. The CSP plants are set in an area with abundant solar energy resources, Phoenix in the USA, in which the annual direct normal irradiance (*DNI*) reaches 7.34 kWh. The annual *DNI* is depicted in Fig. 11(a). Subsequently, the annual solar-thermal power outputs of the CSP plants

integrated with the prototype PTC system and hybrid PTC-PVHC system are calculated and shown in Fig. 11(b) and (c), respectively. It can be observed that the prototype CSP plant harvests lower solar-thermal power output (Table 9) and causes much larger electricity consumption for freezing protection during the off-operation period than the novel hybrid CSP plant. Besides, the PV power output in the novel CSP plant is presented in Fig. 11(d). Though the PV panel is relatively narrow, the total area of PV arrays is pretty considerable due to the long length of the total loops. As a result, the PV arrays generate a substantial power output, contributing to the overall electricity generation of the hybrid CSP plant.

The detailed annual performance metrics are presented in Table 9. The solar-thermal power output of the hybrid CSP plant is higher by 8.0 % than that of the prototype CSP plant. Taking the PV power output into account, the total annual alternating current (AC) power output of the former reaches 245956 MWhe, which is effectively improved by 10.1 % compared to 223435 MWhe in the latter. Furthermore, the hybrid CSP plant exhibits a noteworthy reduction of 87.0% in electricity consumption for annual freeze protection. This significant decrease is primarily attributed to the optimized system design, resulting in a reduced number of loops and a highly effective reduction in heat loss. In the economic aspect, the capital cost of the solar-thermal power system in the hybrid CSP plant is reduced by 4.8% because of its smaller loop number. Considering the additional capital cost of the PV power system, the total net capital cost of the hybrid CSP plant increases to $ 325.5 million but is still lower by 4.0 % than that of the prototype CSP plant, demonstrating the cost advantages of the hybrid CSP plant. As a result, the LCOH and LCOE are calculated. The results demonstrate a noteworthy reduction rate of 14.7% in the LCOH of the solar field within the hybrid CSP plant, which amounts to 1.92¢/kWht compared to the 2.25¢/kWhe observed in the prototype CSP plant. This reduction can be attributed to the enhanced thermal efficiency of the PVHC system and reduced loops, resulting in a higher thermal energy output and reduced operational and maintenance costs. The values of the LCOE of the prototype and hybrid CSP plants are 9.23 and 8.59 ¢/kWhe, respectively, the latter is effectively reduced by 6.9% in comparison to the former. This reduction further emphasizes the economic benefits of the hybrid CSP plant, making it a more cost-effective energy generation option.

Table 9 Annual performance metric of the CSP plants located in Phoenix, with prototype PTC system and hybrid PTC-PVHC system

Item/Metric	Prototype PTC system-based CSP plant	Hybrid PTC-PV system-based CSP plant	Relative improvement/ reduction ratio of the latter over the former
Annual AC power output (MWhe)	**223435**	**245956**	**+10.1 %**
Solar-thermal power output (MWhe)	223435	241339	+8.0 %
Photovoltaic power output (MWhe)	0	4617	\
Annual freeze protection (MWhe)	**26794**	**3486**	**–87.0 %**
Net capital cost ($1M)	**339.0**	**325.5**	**–4.0 %**
Capital cost of the solar-thermal power system ($1M)	339.0	322.6	–4.8 %
Capital cost of the PV power system ($1M)	0	2.9	\
LCOH (¢/kWht)	**2.25**	**1.92**	**–14.7%**
Real LCOE (¢/kWhe)	**9.23**	**8.59**	**–6.9 %**
Real LCOE of the solar-thermal power system (¢/kWhe)	9.23	8.68	–6.0 %
Real LCOE of the PV power system (¢/kWhe)	0	3.98	\

5.4 Configuration and overall performance of the PTC-PVHC system-based 50 MWe CSP plant

Furthermore, to evaluate the techno-economic performance of the hybrid PTC-PVHC system in different weather, three typical areas, namely, Phoenix in the USA, Almería in Spain and Delingha in China, are selected as the locations of the CSP plants. The Phoenix has the best solar irradiance of 7.34 kWh/(m^2·d), and then Almería, Delingha has the worst solar irradiance of 4.23 kWh/(m^2·d). The detailed weather data is presented in Table 10.

Table 10 Weather data of three typical areas

Area	Location	Annual *DNI* (kWh/(m^2·d))	Average ambient temperature (°C)	Average wind speed (m/s)
Phoenix	(111.98°W, 33.45°N), USA	7.34	21.9	1.8
Almería	(2.35°W, 36.85°N), Spain	5.44	19.0	4.1
Delingha	(9.37°E, 37.37°N), China	4.23	4.4	2.1

The calculated results of the annual power outputs and electricity consumption for freeze protection are shown in Fig. 12 and Fig. 13, respectively. It can be seen that the highest annual AC power outputs are observed in Phoenix, while the lowest outputs are observed in Delingha. This correlation confirms that higher solar irradiance directly contributes to increased power generation in CSP plants. However, it is noteworthy that in Delingha, the hybrid CSP plant has the largest improvement ratio of 26.9% from 113493 MWhe in the prototype CSP plant to 144032 MWhe, which is because PTC-PVHC has better thermal efficiency in a scenario of low solar irradiance than that in high solar irradiance (explained in Fig. 10 (b)). In addition, the electricity consumption for freeze protection in the hybrid CSP plant in all three areas is remarkably reduced compared to the prototype CSP plant. Especially in Phoenix, the electricity consumption in the hybrid CSP plant decreased by 87.0 %, demonstrating the superior thermal performance of the PTC-PVHC system.

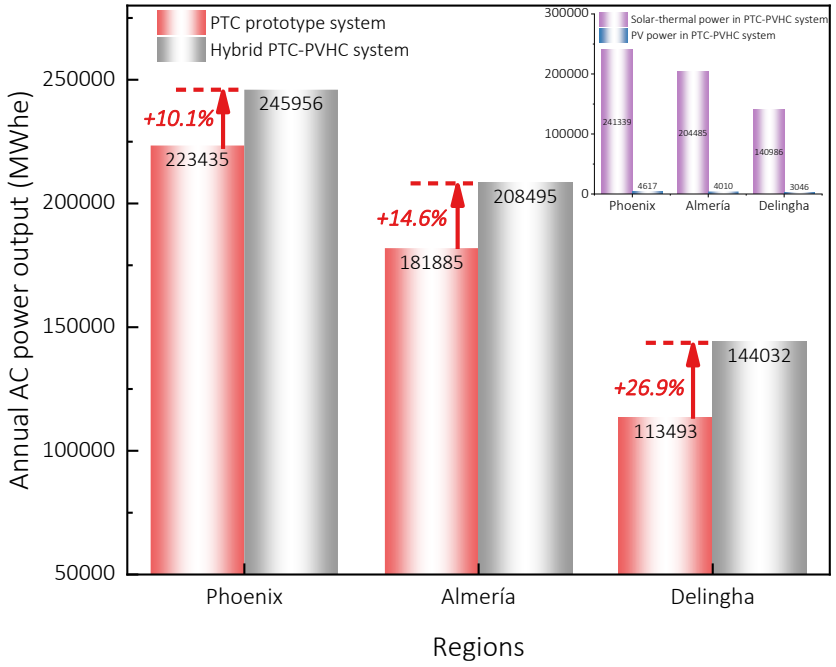

Fig. 12 Annual AC power outputs of prototype and hybrid CSP plants in different regions

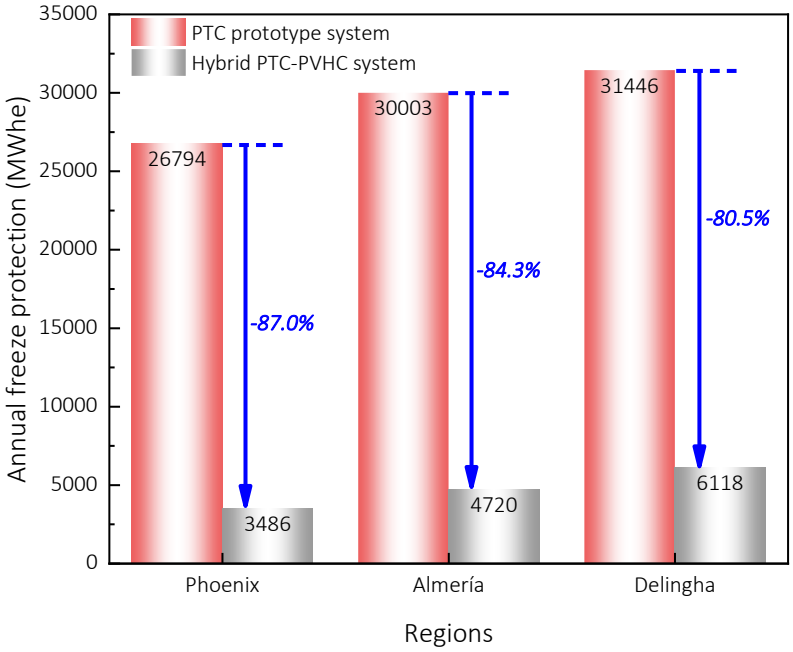

Fig. 13 Annual electricity consumptions for freeze protection in prototype and hybrid CSP plants in different regions

Moreover, the real LCOEs of the prototype and hybrid CSP plants are also calculated and depicted in Fig. 14. Both prototype and hybrid CSP plants in Phoenix have the lowest values of LOCE among three areas, i.e., 9.23 and 8.59 ¢/kWhe, respectively. The latter is effectively reduced by 6.9 % compared to the former. Conversely, the prototype and hybrid CSP plants in Delingha have the highest

LCOE values, with the prototype plant reaching 15.31 ¢/kWh and the hybrid plant at 13.95 ¢/kWh. However, in terms of reduction ratio, the prototype CSP plant in Delingha achieves the largest value of 8.9% compared to the hybrid CSP plant in the same area. All results show that the hybrid CSP plant exhibits pretty superior economic performance than the prototype CSP plant.

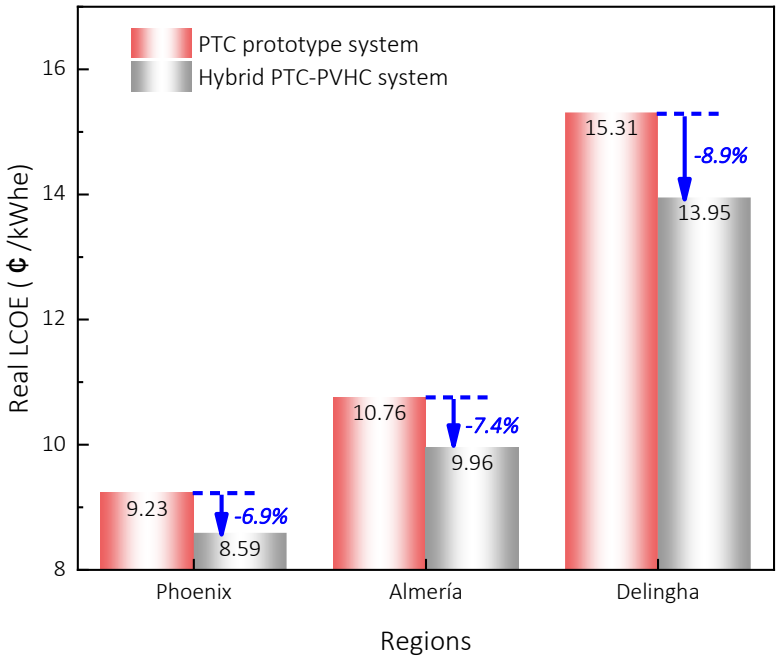

Fig. 14 Real LCOEs of prototype and hybrid CSP plants in different regions

6. Conclusions

In this study, three kinds of configurations of the proposed PTC system integrated with PV panels and aluminum coating (PTC-PVHC) are proposed and tested in the indoor laboratory. The experimental data validates simulation results based on the established mathematical model. The value of *RMSD* well remains within 5 %, demonstrating good prediction ability of the model. Relying on the simulations, the thermal and photoelectrical performance of the PTC-PVHC system is comprehensively evaluated. In addition, the techno-economic metrics of the novel CSP plant with proposed PTC-PVHC are also investigated and analyzed. The main results are summarized as follows.

(1) The aluminum coating exerts effective roles in reducing radiation heat loss of the PTR and lowering the PV temperature. The proposed PTC-PVHC system in this study exhibits superior thermal and photoelectrical performance at higher operating temperatures. The PTC-PVHC

system in the current mode can reduce heat loss by an impressive 45% at the absorber temperature of 600 °C.

(2) The configuration of the PV panel designed in the hybrid PTC-PVHC system has a great advancement in reducing cosine loss, and its efficiency is effectively enhanced by 14.7 % compared to that on the ground. In virtue of the aluminum coating, the hybrid PTC-PVHC system can also effectively improve thermal efficiency by 9.6 % compared to the prototype PTC system in the scenario of low solar irradiance of 300 W/m^2.

(3) The CSP plant integrated with the hybrid PTC-PVHC has superior techno-economic performance than that in the CSP plant with the prototype PTC system. The total annual power output of the former is effectively improved by 10.1 % compared to the latter. Furthermore, the former exhibits a noteworthy reduction of 87.0% in electricity consumption for annual freeze protection. And the LCOH and LCOE of the former are significantly reduced by 14.7 and 6.9 % from the 2.25 ¢/kWht and 9.23 ¢/kWhe in the latter to 1.92¢/kWht and 8.59 ¢/kWhe, respectively.

(4) The hybrid CSP plant has the best techno-economic performance in Delingha, which has the lowest solar irradiance among the three typical areas. In Delingha, the hybrid CSP plant has the largest improvement ratio of 26.9% in annual power output and the most significant reduction ratio of 8.9% in LCOE.

Acknowledgment

This study was sponsored by the RGC Strategic Hiring Scheme (1-BDS2), RGC Postdoctoral Fellowship Scheme 2020/2021 (3-RA59) of the University Grants Committee.

Reference

[1] He Y L, Qiu Y, Wang K, et al. Perspective of concentrating solar power[J]. Energy, 2020, 198: 117373.

[2] Nie F, Bai F, Wang Z, et al. Solid particle solar receivers in the next-generation concentrated solar power plant[J]. EcoMat, 2022, 4(5): e12207.

[3] Mao Z, Yao Y, Shen J, et al. Passive interfacial cooling-induced sustainable electricity–water cogeneration[J]. Nature Water, 2024: 1-8.

[4] Yadav V K, Sarkar J, Ghosh P. Thermodynamic, economic and environmental analyses of novel concentrated solar-PV-thermal integrated combined power, cooling and desalination system[J]. Desalination, 2023: 116721.
[5] Yang Y, Feng H, Que W, et al. A Diode-like Scalable Asymmetric Solar Evaporator with Ultra-high Salt Resistance[J]. Advanced Functional Materials, 2023, 33(6): 2210972.
[6] Liu P, Ren T T, Ge Y L, et al. Performance analyses of a novel finned parabolic trough receiver with inner tube for solar cascade heat collection[J]. Science China Technological Sciences, 2023, 66(5): 1417-1434.
[7] Xia Q, Qiu H, Wang J, et al. Efficient distributed concentrating solar power system with ammonia-based chemical heat pump[J]. Energy Conversion and Management, 2023, 276: 116575.
[8] Wang Q, Yang H, Zhong S, et al. Comprehensive experimental testing and analysis on parabolic trough solar receiver integrated with radiation shield[J]. Applied Energy, 2020, 268: 115004.
[9] Shi X, Zhao X, Wang F, et al. Improving overall heat transfer performance of parabolic trough solar receiver by helically convex absorber tube[J]. Applied Thermal Engineering, 2022, 213: 118690.
[10] Wang Q, Yang H, Hu M, et al. Optimization strategies and verifications of negative thermal-flux region occurring in parabolic trough solar receiver[J]. Journal of Cleaner Production, 2021, 278: 123407.
[11] Wang K, Li Y F, Zhang Z D, et al. Convective heat transfer characteristics of supercritical CO2 in mini-channels of compact solar receivers under unilateral heating conditions[J]. Applied Thermal Engineering, 2023: 120862.
[12] Bellos E, Said Z, Lykas P, et al. A review of polygeneration systems with CO2 working fluid[J]. Thermal Science and Engineering Progress, 2022: 101435.
[13] Wang Q, Yao Y, Shen Z, et al. Concentrated solar power tower systems coupled locally with spectrally selective coatings for enhancement of solar-thermal conversion and economic performance[J]. Green Energy and Resources, 2023, 1(1): 100001.
[14] Häberle A. Linear fresnel collectors[M]//Solar Thermal Energy. New York, NY: Springer US, 2022: 55-62.
[15] Brandão A S M, da Costa Mendes P R, Normey-Rico J E. Simplified optical model, aiming strategy and partial defocusing strategy for solar Fresnel collectors[J]. Renewable Energy, 2022, 188: 11-36.
[16] Kumar K H, Daabo A M, Karmakar M K, et al. Solar parabolic dish collector for concentrated solar thermal systems: a review and recommendations[J]. Environmental Science and Pollution Research, 2022, 29(22): 32335-32367.
[17] Liang H, Su R, Huang W, et al. A novel spectral beam splitting photovoltaic/thermal hybrid system based on semi-transparent solar cell with serrated groove structure for co-generation of electricity and high-grade thermal energy[J]. Energy Conversion and Management, 2022, 252: 115049.
[18] Huang S, Yu H, Zhang M, et al. Advances, challenges and outlooks in frost-free air-source heat pumps: A comprehensive review from materials, components to systems[J]. Applied Thermal Engineering, 2023: 121163.

[19] Pitz-Paal R. Concentrating solar power: still small but learning fast[J]. Nature Energy, 2017, 2(7): 1-2.
[20] Wang Q, Shen B, Huang J, et al. A spectral self-regulating parabolic trough solar receiver integrated with vanadium dioxide-based thermochromic coating[J]. Applied Energy, 2021, 285: 116453.
[21] Qiu Y, Xu Y, Li Q, et al. Efficiency enhancement of a solar trough collector by combining solar and hot mirrors[J]. Applied Energy, 2021, 299: 117290.
[22] Bellos E, Tzivanidis C, Tsimpoukis D. Thermal, hydraulic and exergetic evaluation of a parabolic trough collector operating with thermal oil and molten salt based nanofluids[J]. Energy Conversion and Management, 2018, 156: 388-402.
[23] Wan Z, Wei J, Qaisrani M A, et al. Evaluation on thermal and mechanical performance of the hot tank in the two-tank molten salt heat storage system[J]. Applied Thermal Engineering, 2020, 167: 114775.
[24] Padilla R V, Demirkaya G, Goswami D Y, et al. Heat transfer analysis of parabolic trough solar receiver[J]. Applied energy, 2011, 88(12): 5097-5110.
[25] Burkholder F, Kutscher C. Heat loss testing of Schott's 2008 PTR70 parabolic trough receiver[R]. National Renewable Energy Lab.(NREL), Golden, CO (United States), 2009.
[26] Yu H, Zhang Y, Zhang Q, et al. Microstructure and Thermal Stability of Cu/TixSiyN/AlSiN Solar Selective Absorbing Coating[J]. Materials, 2020, 13(4): 882.
[27] Zhao K, Jin H, Gai Z, et al. A thermal efficiency-enhancing strategy of parabolic trough collector systems by cascadingly applying multiple solar selective-absorbing coatings[J]. Applied Energy, 2022, 309: 118508.
[28] Xu K, Du M, Hao L, et al. A review of high-temperature selective absorbing coatings for solar thermal applications[J]. Journal of Materiomics, 2020, 6(1): 167-182.
[29] Niranjan K, Krause M, Lungwitz F, et al. WAlSiN-based solar-selective coating stability-study under heating and cooling cycles in vacuum up to 800° C using in situ Rutherford backscattering spectrometry and spectroscopic ellipsometry[J]. Solar Energy Materials and Solar Cells, 2023, 255: 112305.
[30] Thappa S, Chauhan A, Sawhney A, et al. Thermal selective coatings and its enhancement characteristics for efficient power generation through parabolic trough collector (PTC). Clean Technologies and Environmental Policy, 2020: 1-21.
[31] Wang Q, Yang H, Zhong S, et al. Quantitative analyses and a novel optimization strategy on negative energy-flow region in parabolic trough solar receivers[J]. Solar Energy, 2020, 196: 663-672.
[32] Hu T, Kwan T H, Zhang H, et al. Thermal performance investigation of the newly shaped vacuum tubes of parabolic trough collector system[J]. Energy, 2023, 278: 127802.
[33] Yang H, Wang Q, Huang Y, et al. Spectral optimization of solar selective absorbing coating for parabolic trough receiver[J]. Energy, 2019, 183: 639-650.
[34] Al-Ansary H, Zeitoun O. Numerical study of conduction and convection heat losses from a half-insulated air-filled annulus of the receiver of a parabolic trough collector[J]. Solar Energy, 2011, 85(11): 3036-3045.

[35] Wang Q, Li J, Yang H, et al. Performance analysis on a high-temperature solar evacuated receiver with an inner radiation shield[J]. Energy, 2017, 139: 447-458.
[36] Li Q, Zhang Y, Wen Z X, et al. An evacuated receiver partially insulated by a solar transparent aerogel for parabolic trough collector[J]. Energy Conversion and Management, 2020, 214: 112911.
[37] Wang Q, Yao Y, Shen Z, et al. A hybrid parabolic trough solar collector system integrated with photovoltaics[J]. Applied Energy, 2023, 329: 120336.
[38] Li G, Lu Y, Zhao X. The Gaussian non-uniform temperature field on PV cells-A unique solution for enhancing the performance of the PV/T module[J]. Energy, 2022, 250: 123621.
[39] Hu M, Zhao B, Ao X, et al. Applications of radiative sky cooling in solar energy systems: Progress, challenges, and prospects[J]. Renewable and Sustainable Energy Reviews, 2022, 160: 112304.
[40] Montañés R M, Windahl J, Pålsson J, et al. Dynamic modeling of a parabolic trough solar thermal power plant with thermal storage using modelica[J]. Heat Transfer Engineering, 2018, 39(3): 277-292.
[41] Wang Q, Huang J, Shen Z, et al. Negative thermal-flux phenomenon and regional solar absorbing coating improvement strategy for the next-generation solar power tower[J]. Energy Conversion and Management, 2021, 247: 114756.
[42] Awad A, Navarro H, Ding Y, et al. Thermal-physical properties of nanoparticle-seeded nitrate molten salts[J]. Renewable Energy, 2018, 120: 275-288.
[43] Benidir A, Khaldi F, Benmachiche A H, et al. Numerical thermal analysis of Schott 2008 PTR70 solar receiver under hassi R'mel power plant operation conditions[J]. Journal of Engineering Science and Technology, 2018, 13(1): 122-140.
[44] Geyer M, Lüpfert E, Osuna R, et al. EUROTROUGH-Parabolic trough collector developed for cost efficient solar power generation[C]//11th International symposium on concentrating solar power and chemical energy technologies. 2002: 04-06.
[45] Wang Q, Pei G, Yang H. Techno-economic assessment of performance-enhanced parabolic trough receiver in concentrated solar power plants[J]. Renewable Energy, 2021, 167: 629-643.
[46] Gharat P V, Bhalekar S S, Dalvi V H, et al. Chronological development of innovations in reflector systems of parabolic trough solar collector (PTC)-A review[J]. Renewable and Sustainable Energy Reviews, 2021, 145: 111002.
[47] Hu M, Zhao B, Cao J, et al. Feasibility of realizing daytime solar heating and radiative cooling simultaneously with a novel structure[J]. Sustainable Cities and Society, 2021, 74: 103224.
[48] Kacira M, Simsek M, Babur Y, et al. Determining optimum tilt angles and orientations of photovoltaic panels in Sanliurfa, Turkey[J]. Renewable energy, 2004, 29(8): 1265-1275.
[49] Bellos E, Tzivanidis C, Belessiotis V. Daily performance of parabolic trough solar collectors[J]. Solar Energy, 2017, 158: 663-678.
[50] Wang Q, Li G, Cao J, et al. An analytical study on optimal spectral characters of solar absorbing coating and thermal performance potential of solar power tower[J]. Renewable Energy, 2022, 200: 1300-1315.

[51] Fesharaki V J, Dehghani M, Fesharaki J J, et al. The effect of temperature on photovoltaic cell efficiency[C]//Proceedings of the 1stInternational Conference on Emerging Trends in Energy Conservation–ETEC, Tehran, Iran. 2011: 20-21.

[52] Blair N, Dobos A P, Freeman J, et al. System advisor model, sam 2014.1. 14: General description. National Renewable Energy Lab. (NREL), Golden, CO (United States), 2014.

[53] Wang Q, Yao Y, Hu M, et al. An air curtain surrounding the solar tower receiver for effective reduction of convective heat loss[J]. Sustainable Cities and Society, 2021, 71: 103007.

[54] Islam M T, Huda N, Saidur R. Current energy mix and techno-economic analysis of concentrating solar power (CSP) technologies in Malaysia. Renewable energy 2019; 140: 789-806.

[55] Delise T, Tizzoni A C, Menale C, et al. Technical and economic analysis of a CSP plant presenting a low freezing ternary mixture as storage and transfer fluid. Applied Energy 2020; 265: 114676.

[56] Turchi, C. S. (2010). "Parabolic Trough Reference Plant for Cost Modeling with the Solar Advisor Model (SAM)," NREL/TP-550-47605.

[57] Gabbrielli R, Castrataro P, Del Medico F, et al. Levelized cost of heat for linear Fresnel concentrated solar systems[J]. Energy Procedia, 2014, 49: 1340-1349.

[58] Alhejji A, Kuriqi A, Jurasz J, et al. Energy harvesting and water saving in arid regions via solar PV accommodation in irrigation canals[J]. Energies, 2021, 14(9): 2620.

[59] Shouman E R, Khattab N M. Future economic of concentrating solar power (CSP) for electricity generation in Egypt. Renewable and Sustainable Energy Reviews 2015; 41: 1119-1127.

[60] Carlin T M, Finch N, Schauten M, et al. The discount rate for discounted cash flow valuations of intangible assets. Managerial Finance, 2010.

[61] Ma T, Yang H, Gu W, et al. Development of walkable photovoltaic floor tiles used for pavement[J]. Energy Conversion and Management, 2019, 183: 764-771.

[62] IEC. 60904-9 Photovoltaic devices Part 9: Solar simulator performance requirements 2008.

[63] Algareu AO. Development of reflective low concentrated photovoltaic/thermal system [Ph.D.]. University of Birmingham; 2017.

[64] Halimi M, Outana I, El Amrani A, et al. Prediction of captured solar energy for different orientations and tracking modes of a PTC system: Technical feasibility study (Case study: South eastern of MOROCCO). Energy Conversion and Management 2018; 167: 21-36.

[65] Wang Q, Hu M, Yang H, et al. Performance evaluation and analyses of novel parabolic trough evacuated collector tubes with spectrum-selective glass envelope[J]. Renewable Energy, 2019, 138: 793-804.